

## Research Article

# Synthesis and Properties of a Reinforcing Dust-Cementing Material for Thin Spray-On Liners in Mine Roadways

Gang Zhou <sup>1,2,3</sup> Shuailong Li <sup>1,2</sup> Yunlong Ma <sup>1,2</sup> Jianfei Ding <sup>1,2</sup>  
and Mingguang Zhang <sup>1,2</sup>

<sup>1</sup>College of Mining and Safety Engineering, Shandong University of Science and Technology, Qingdao 266590, China

<sup>2</sup>State Key Laboratory of Mining Disaster Prevention and Control Co-founded by Shandong Province and the Ministry of Science and Technology, Shandong University of Science and Technology, Qingdao 266590, China

<sup>3</sup>Energy Flagship, Commonwealth Scientific and Industrial Research Organisation, P.O. Box 883, Kenmore, Brisbane, QLD 4069, Australia

Correspondence should be addressed to Shuailong Li; 17051873444@163.com

Received 10 May 2018; Accepted 9 January 2019; Published 4 February 2019

Academic Editor: Michael Aizenshtein

Copyright © 2019 Gang Zhou et al. This is an open access article distributed under the Creative Commons Attribution License, which permits unrestricted use, distribution, and reproduction in any medium, provided the original work is properly cited.

The sprayed concrete in mine roadways suffers from a prolonged exposure to the harsh environment in the underground mine, leading to its detachment which may compromise its supporting strength. Besides, the dust-cementing effect of the conventional concrete is poor, providing very limited contribution to suppress the dust-laden airflow. As such, the present experiment uses sodium carboxymethyl cellulose as the base to produce a novel thin spray material through graft copolymerization based on acrylic acid and polyaluminum chloride. This new material can not only reinforce the surrounding rock of the roadway but also cement the dust in the airflow. Infrared spectroscopy, X-ray diffraction, thermal gravimetric analysis, and SEM are employed collectively to study the microscale reaction and structure of the product. A suite of experiment testing is carried out concerning the performance of the developed spray material, which reveals the supreme mechanical strength and desired properties of the hardened film developed from the spray material.

## 1. Introduction

Due to the harsh environment in the underground mine with high stress, high temperature, high humidity, and persistent ventilation, the surrounding rock of the roadway is subject to weathering [1–3]. The anchor network also suffers from severe corrosion, which compromises the reinforcement strength. After setting up the anchor network for supporting the surrounding rock, concrete or mortar is sprayed onto it for providing isolation and protection against weathering. However, the sprayed concrete or mortar may undergo large-scale detachment, which constitutes a major threat to the stability of the roadway. It may significantly shorten the service time of the roadway and compromise the safety of production. To address this issue, one may supplement concrete, mortar, or cement spray

locally to reinforce the supporting strength. However, this operation is labor-intensive and material-consuming [4]. Besides, the subsurface ventilation not only causes the airflow to carry certain amount of dust into the roadway but also may induce reentrainment of the deposited dust [5]. The dust-laden airflow entering the excavation zone poses a heinous threat to the occupational safety of the miners [6, 7]. For this reason, spray of rock dust, cleaning, and cement swabbing have to be applied to the roadway on a periodical basis to suppress the dispersion of the dust. These measures are notoriously water-, labor-, and material-consuming and give rise to a hostile working environment. Therefore, it is of paramount importance to develop a novel concrete spray that can be applied in a quick, cost-effective, and environmentally friendly manner and can help suppress the dust dispersion in the roadway [8–10].

Since 2009, Chinese scholars have been conducting active research on developing thin spray materials for coal mines. Significant progresses have been made concerning the thin spray-on techniques with antiweathering, anticorrosion, and antigas natures in refuge chambers. Progresses are also made concerning the thermal isolation in deep mines and the substitutes for the anchored net [11–13]. However, most of the developed techniques are based on adding materials to the liquid cement instead of developing brand new materials from the scratch. The research of the thin spray material starts early in western countries, e.g., Germany, America, Australia, and Canada. The corresponding mechanisms can be divided into two types, i.e., reaction-based and nonreaction-based [14, 15]. The reaction-based techniques mainly refer to the polyurethane/polyurea system, whose advantage lies in its strong ability to establish a hardened film with decent strength. However, these techniques have to deal with the temperature increase issue during reaction, as well as the high equipment cost and complicated operating workflow. Most nonreaction techniques rely on cement-based materials, which modify the property of the cement by adding polymer to it. Despite the low cost, these techniques give rise to a hardened film with an array of disadvantages, including high fragility, low adherence force, and poor durability.

Presently, with the advancement of the exploration and recovery technology, the subsurface mining operation has to deal with increasingly complicated geologic and environmental conditions. Given this situation, one not only needs to find an effective way to reinforce the surrounding rock but also needs to protect the roadway surrounding rock from weathering, airflow leakage, and self-ignition [16–18]. Built on the top of the conventional concrete spray methodology, there exists an urgent need to develop a fast, effective, and high-strength spray material for the postprocessing step so as to provide secondary reinforcement and protection to the anchor network. The present research is inspired by the product of the graft copolymerization, which refers to the technology for grafting a composite with a distinct chemical structure to certain atoms on the backbone of the polymer to form a copolymer. Through graft modification, one can equip the base material with some unique properties [19, 20]. Currently, the graft copolymerization technology has been widely applied to diverse areas in the coal mining industry. For instance, Fan et al. [21] applied graft copolymerization using lignin sulfonate as the base to synthesize a novel cementing agent for suppressing dust in coal mines; Spagnol et al. [22] used chitosan-grafted polyacrylic acid/ash-based husk to prepare the highly water-absorbing hydrogel composite material. As for the study on roadway thin spray materials, Ozturk [23] conducted systematic tests on the adhesion geometry model and failure model associated with a thin spray material; Mpunzi et al. [24] proved experimentally that the thin spray material can enhance the tensile strength of the rock and spray concrete; and Guner and Ozturk [25] studied the tensile mechanical property of the thin spray material through the hardening experiment and numerical analysis. However, there exist few reports on the application of thin spray materials to the coal mine roadway.

The present research uses sodium carboxymethyl cellulose as the base, which is reacted with the acrylic acid through graft modification for producing the intermediate product. The intermediate product in turn reacts with polyaluminum chloride through the coordination chelating effect to generate a potent spray material. Applying this material to the concrete and wire mesh surface can provide secondary reinforcement to the surrounding rock, prevent airflow leakage in the roadway, and slow down the corrosion of the wire mesh. Subsequently, infrared spectroscopy, thermal gravimetric analysis, X-ray diffraction, and SEM techniques are employed to analyze the microscale reaction and structure of the developed product; a hardness test on the developed hardened film is carried out to investigate the antiweathering performance of the product; a tensile strength test is conducted to show the product's ability to withstand the external force; anticompression and antibending tests are performed to test the protective ability of the product; an adhesive effect test is conducted to study the product's ability to absorb dust; and a cementing test is utilized to illustrate the product's ability to trap the entrained dust in the roadway airflow.

## 2. Materials and Experimental Procedures

*2.1. Raw Materials.* The raw materials are sodium carboxymethyl cellulose, acrylic acid, ammonium persulfate, polyaluminum chloride, sodium hydroxide, hydrochloric acid (the aforementioned materials are all purchased from the Qingdao Fine Chemicals Co., Ltd., and are all of AR grade), and distilled water (self-prepared).

*2.2. Experimental Procedure.* The product is prepared following the steps below: place a beaker with 300 ml water in a water bath; set the temperature to 50°C; add acrylic acid to the beaker with 60% neutrality; On stirring continuously, slowly add a small amount of sodium carboxymethyl cellulose to the beaker; after a complete dissolution of the sodium carboxymethyl cellulose, place the reactants in a blender filled with nitrogen for protection; properly set the reaction temperature, and then add ammonium persulfate; let the reaction continue for two hours; dissolve certain amount of polyaluminum chloride in a small beaker, and slowly pour the polyaluminum chloride solution into the beaker with reactants; and keep stirring for 1 hour, and the final product is obtained.

*2.3. Impact of Single Factor on the Final Product.* During the preparation of the spray material, the composition of the reactants has a major impact on the resulting performance of the product. Specifically, the contents of acrylic acid, initiator ammonium persulfate, and polyaluminum chloride, as well as reaction temperature, affect the properties of the product considerably. The present experiment uses 2.5 grams of sodium carboxymethyl cellulose as the base and designs a suite of single-factor experiments based on using the hardness of the established film as a performance indicator for studying the impact of the reactant composition on the prepared product. Table 1 is list of single-factor experiments.

TABLE 1: List of single-factor experiments.

Experiment ID	CMC (g)	AA (ml)	APS/AA (%)	PAC/CMC (%)	Temperature (°C)
0	0	2	2	20	50
1	2.5	1	2	20	50
2	2.5	2	2	20	50
3	2.5	3	2	20	50
4	2.5	4	2	20	50
5	2.5	5	2	20	50
6	2.5	4	0.5	20	50
7	2.5	4	1	20	50
8	2.5	4	1.5	20	50
9	2.5	4	2	20	50
10	2.5	4	2.5	20	50
11	2.5	4	2	10	50
12	2.5	4	2	15	50
13	2.5	4	2	20	50
14	2.5	4	2	25	50
15	2.5	4	2	30	50
16	2.5	4	2	20	30
17	2.5	4	2	20	40
18	2.5	4	2	20	50
19	2.5	4	2	20	60
20	2.5	4	2	20	70

Note: CMC, sodium carboxymethyl cellulose; AA, acrylic acid; APS, ammonium persulfate; PAC, polyaluminium chloride.

**2.4. Fourier Transform Infrared Analysis Experiment.** In order to analyze the change of photogroups of products, the reaction mode between the test agents was deduced. Place CMC and the final product in a vacuum drying chamber for a 24-hour desiccation at 90°C; subsequently, put the dried material in a mortar for a thorough grinding; subject the resulting mesh of 200 particles to an infrared spectroscopy test by (1) mixing the two materials with KBr, (2) grinding and then making a thin slice by press, and (3) placing the prepared thin slice in a NICOLET iS10 Fourier transform infrared spectrometer to conduct the infrared experiment for studying the variation of the functional groups.

**2.5. Thermogravimetric Analysis.** Analyze the thermal stability and thermal decomposition of materials. Put the final product in a vacuum drying chamber for desiccation. Put 5–8 mg of solid powder inside a Mettler TGA/DSC 1 1600HT thermogravimetric analyzer. During the experiment, the heating rate is set at 20°C·min<sup>-1</sup>, and the temperature range is set at 20–650°C.

**2.6. XRD Experiment.** For further analysis of product crystallinity, put the desiccated sample inside a mortar for grinding until the particle size meets the requirement. Prepare a XRD scanning pellet and put it into a Bruker D2 PHASER X-ray analyzer for scanning. The scanning angle is 10°–70°, and the scanning rate is 4°/min. This experiment generates the XRD spectra of the raw material and the final product for comparison.

**2.7. Scanning Electron Microscope (SEM).** To observe the microstructures of the products, infer the way in which they

act. Put the final product in a vacuum drying chamber for desiccation, followed by pulverization. Put the pulverized sample in a ZEISS MERLIN Compact SEM for scanning. The experimental results show the microscopic structure of the product.

## 2.8. Product Characteristics Tests

### 2.8.1. Reinforcement Performance

(1) *Tensile Strength Test.* Place a layer of plastic membrane at the bottom of a Petri dish (diameter 7 cm) and then put the product in its liquid state in the Petri dish. Put the sample in a drying chamber at 55°C for 5–6 hours. Take out the formed thin film and remove the plastic membrane at the bottom. The prepared thin film is 7 cm in diameter and 5 mm thick. The prepared product was clamped to the upper end with a mold of a WDS-5 type digital display universal testing machine, and then the bottom was fixed, and the moving speed was set to 5 mm/min, and the tensile strength of the test product was measured. PAC/CMC were 5%, 10%, 15%, 20%, 25%, and 30%, respectively.

(2) *Adhesive Force Test.* A viscometer is employed to measure the viscosity coefficient of the product. Then place 10 g, 20 g, 30 g, 40 g, and 50 g of product samples between two 5 cm × 5 cm × 5 cm concrete plates. After desiccation, conduct tensile testing with a TFW-10S computerized electronic universal testing machine. Set the testing speed to 10 mm/min. This test can directly reveal the adhesion between product and concrete. Figure 1 shows the schematic diagram of the test, and various amounts of the product are placed between two cement slabs.

(3) *Anticompression and Antibending Strengths.* To further illustrate the strength of the product, we conduct the following experiment: put a thoroughly desiccated round sample (3 cm in diameter and 5 mm thick) in a TFW-10S computerized electronic universal testing machine and conduct compression and antibending tests at 100 mm/min.

### 2.8.2. Dust-Cementing Performance

(1) *Dust-Cementing Test.* Evenly spray the final product (liquid state) over a 25 cm by 12 cm coarse plastic slab, forming a 2 mm thick film. Then, evenly spray 3 grams of fat coal powder (over 100-mesh sieve) over the plastic slab. Use a fan to blow cement board for 3 minutes at a different wind speed along the horizontal direction at one end of cement. Finally use the weight gain of the plastic slab as the metric to measure the dust-absorbing effect after 3 days and 7 days of desiccation, respectively.

(2) *Observation with an Industrial Camera.* Place the sample with three days of desiccation and dust cementing under a CCD camera and set the magnification ratio to different values. Observe the dust-cementing effect under various

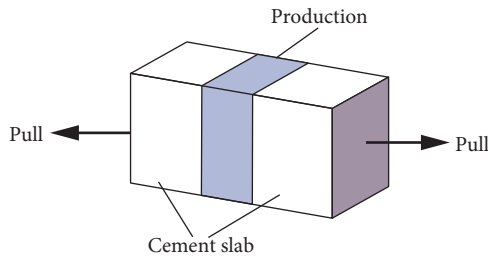


FIGURE 1: Schematic diagram of the test.

magnification ratios. This observation can reveal the microscopic dust cementing mechanism.

### 3. Experimental Results and Discussion

#### 3.1. Single-Factor Experimental Analysis

**3.1.1. Impact of Acrylic Acid on the Hardness of the Formed Film.** Figure 2(a) shows how the amount of acrylic acid affects the hardness of the formed film. With the increase of the acrylic acid amount, the hardness of the formed film increases first and then decreases. Meanwhile, the amount of free radicals in the solution also increase, which enhance the grafting rate of the reaction and reinforce the molecular structure. As a result, the hardness of the formed film increases accordingly. As the amount of acrylic acid exceeds 4 ml, the amount of primer in the reaction remains stable, yet the free radicals are able to consume some primer during the self-polymerization, which reduces the stability of the product due to the reduction of primer. As a result, the hardness of the formed film drops.

**3.1.2. Impact of Initiator on the Hardness of the Formed Film.** Figure 2(b) shows the impact of initiator amount on the hardness of the formed film. With the increase of initiator amount, the amount of primer in the solution also increases, which makes the reaction in the solution more complete. The free radicals bond with primer, forming a stable structure. Therefore, the hardness of the formed film is enhanced. When the ratio of the initiator to acrylic acid exceeds 2%, there exist excessive free radicals in the solution that cannot be consumed by the reaction. Instead, these residual free radicals undergo self-polymerization, making the product structure relatively loose with reduced hardness of the formed film.

**3.1.3. Impact of Cross-Linking Agent on the Hardness of the Formed Film.** Figure 2(c) shows the impact of cross-linking agent amount on the hardness of the formed film. With the increase of the cross-linking agent, the coordinated reaction is accelerated. The product generated through coordination keys is more stable, leading to an enhanced hardness of the formed film. After the amount of the cross-linking agent reaches a certain level, a further increase of it fails to cause a major increase of the film hardness. This is due to the fact that a further increase of the cross-linking agent leads to more invalid coordination reaction, which consumes a

portion of the monomers. Therefore, the hardness of the formed film does not increase significantly anymore.

**3.1.4. Impact of Temperature on the Film Hardness.** Figure 2(d) shows how the variation of temperature affects the film hardness. With the increase of temperature, the primer and free radicals in the solution become more active, leading to a boost of reaction rate and effectiveness. As such, the hardness of the film is enhanced. When temperature exceeds 50°C, the rates of reaction and decomposition in the solution are high, which causes the cross-linking and self-polymerization to occur concurrently. The formed molecular structure becomes unstable, making the film hardness of the product compromised.

Through a suite of single-factor experiments, it is determined that the optimal formula is sodium carboxymethyl cellulose: acrylic acid = 5 : 8, initiator: acrylic acid = 2.0%, and cross-linking agent: sodium carboxymethyl cellulose = 1 : 5. The optimal reaction temperature is 50°C.

**3.2. Infrared Analysis.** Figure 3 shows the infrared spectra of the final product (CMC-AA-PAC) and the base (CMC). Analysis indicates that the two curves in the figure both exhibit an absorption peak associated with the O-H stretching vibration near 3419  $\text{cm}^{-1}$ ; the strong adsorption band at 1597  $\text{cm}^{-1}$  belongs to the absorption peak of antisymmetrical stretching vibration associated with the carboxylic acid ion in the CMC-Na salt; and through graft copolymerization, it can be found in the CMC-AA-PAC curve that the tensile absorption peak of the hydroxy group -OH in the sodium carboxymethyl cellulose is split into two absorption peaks, i.e., 3447  $\text{cm}^{-1}$  and 3400  $\text{cm}^{-1}$ . This observation proves that the grafting occurs with the reaction between acrylic acid and the sodium carboxymethyl cellulose. As shown in Figures 4(a) and 4(b), through the influence of the initiator and heating, the -OH in sodium carboxymethyl cellulose is activated. The addition of acrylic acid then breaks up the C=C double bond, which are in turn grafted to the -O<sup>-</sup> in the sodium carboxymethyl cellulose; an absorption peak of -Al-O stretching vibration appears at 615  $\text{cm}^{-1}$ , and the antisymmetrical stretching vibration peak of -COO<sup>-</sup> shifts from 1597  $\text{cm}^{-1}$  to 1623  $\text{cm}^{-1}$ . The ionization of CMC-Na salt generates a multitude of  $\pi$  bond systems, causing the resonance to occur between two C-O bonds. After the cross-linking with the polyaluminum chloride occurs, the original  $\pi$  bond system is compromised, and the asymmetrical vibration peak of COO<sup>-</sup> migrates. This indicates that the carboxylic acid participates in the coordination, which further proves the existence of the -C-O-Al-. The shift of the peak to the high frequency side of the spectrum indicates the presence of the coordination of the carboxyl system, as shown in Figures 4(c) and 4(d). The Al<sup>3+</sup> cross-linking gives rise to a three-dimensional network structure [26].

**3.3. Thermogravimetric Analysis.** The TG-DSC curve of the final product is shown in Figure 5. Specifically, the TG-DSC

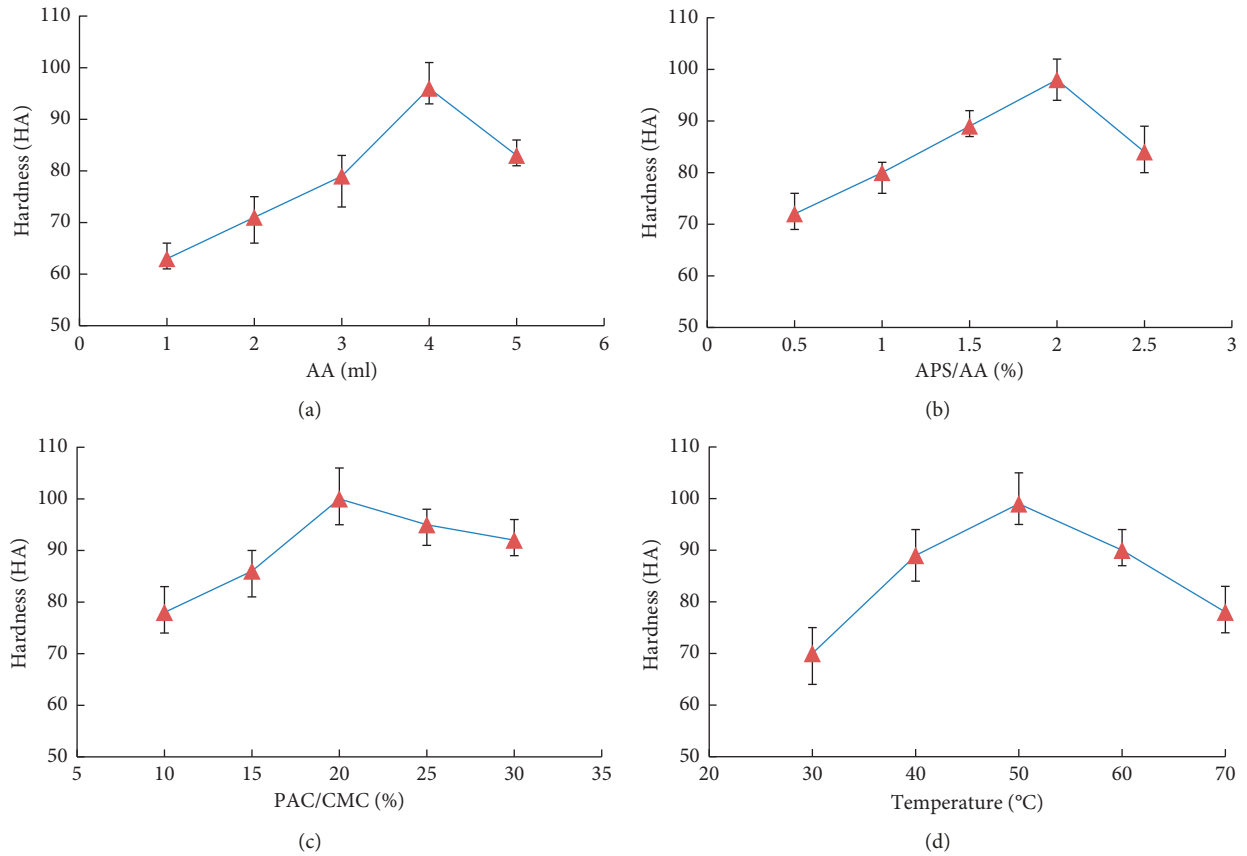


FIGURE 2: The factors that affect the hardness of film forming.

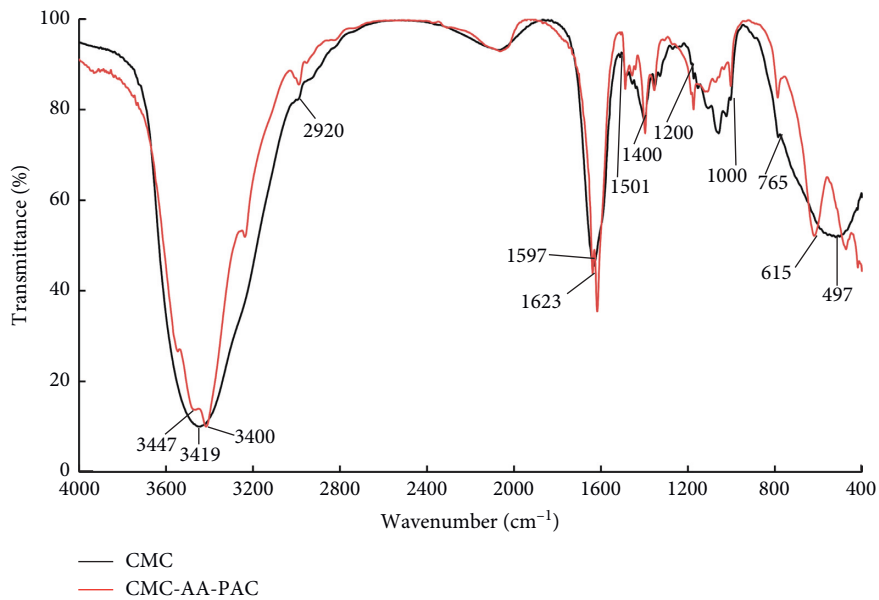


FIGURE 3: Transmittance vs. wave number derived from infrared analyses of product.

curve has three stages: In the first stage (<185°C), the mass loss is mainly caused by the evaporation of free water and crystal water in the network structure of the product, leading to 8.1% mass loss; the second stage (202°C–401°C) experiences the highest mass loss, which is mainly driven by the

water loss in the polysaccharides chain and the rupture of the C-O-C glycoside chain in the sodium carboxymethyl cellulose, leading to 21.50% mass loss; and the third stage occurs between 414°C and 471°C, corresponding to 13.3% mass loss, which is due to the further oxidation of the

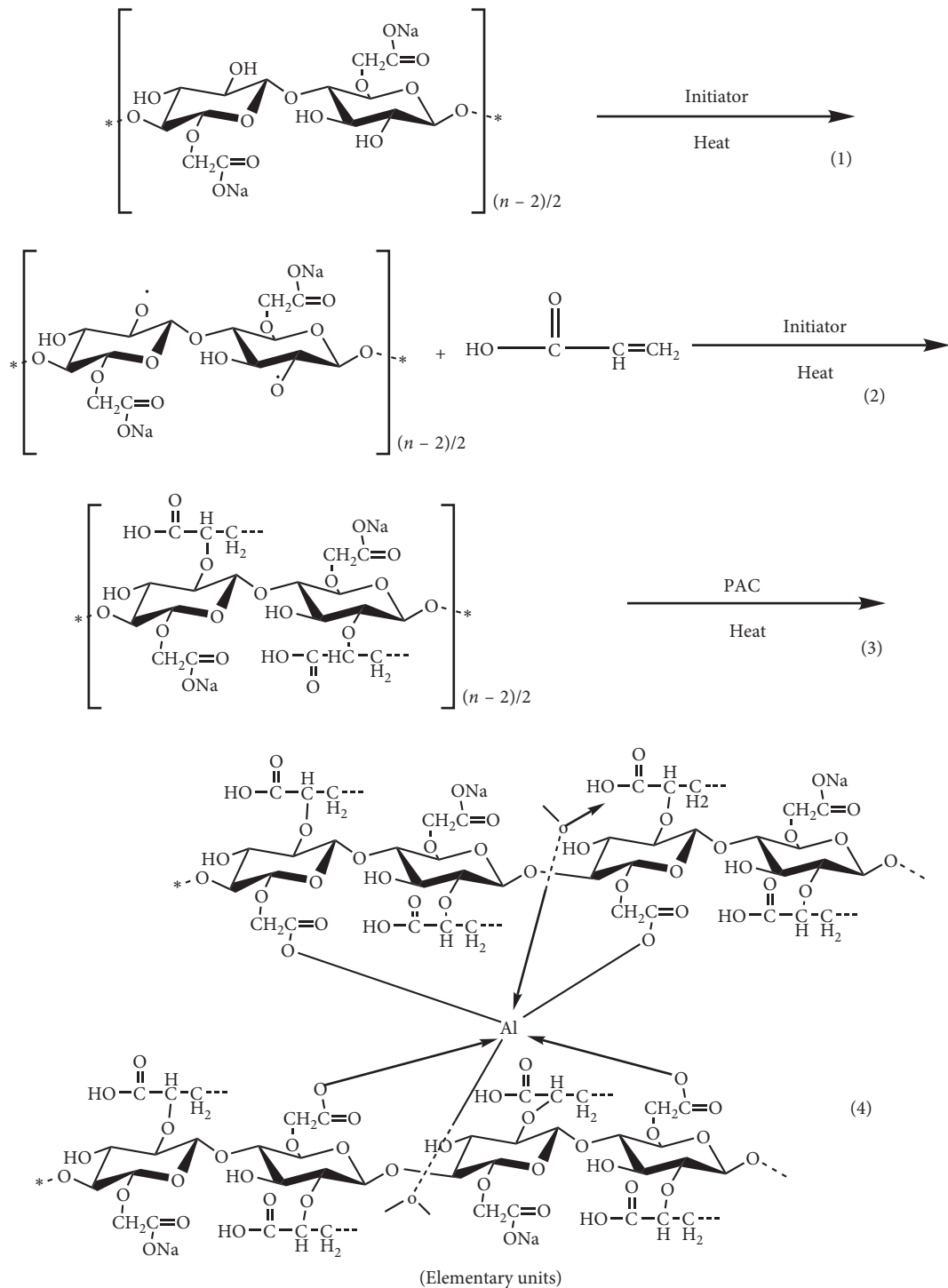


FIGURE 4: Mechanism of product preparation.

carbonized product. An examination of the overall curve indicates that the mass change of the product during the thermogravimetric analysis is insignificant [27].

Under the normal condition, a temperature gradient exists in the surrounding rock of the underground mine roadway. At a depth of 1000 m, the temperature of the roadway surrounding rock is approximately 43°C. Therefore, the spray of the product on the roadway surrounding rock would not cause structural damage due to excessive increase

of temperature, and the thermal stability of the product is basically ensured.

**3.4. XRD Analysis.** The X-ray diffraction spectra of sodium carboxymethyl cellulose and final product are shown in Figure 6. It is found that a “steamed bun peak” exists in the spectrum of sodium carboxymethyl cellulose, which is the characteristic peak associated with the polymer. This

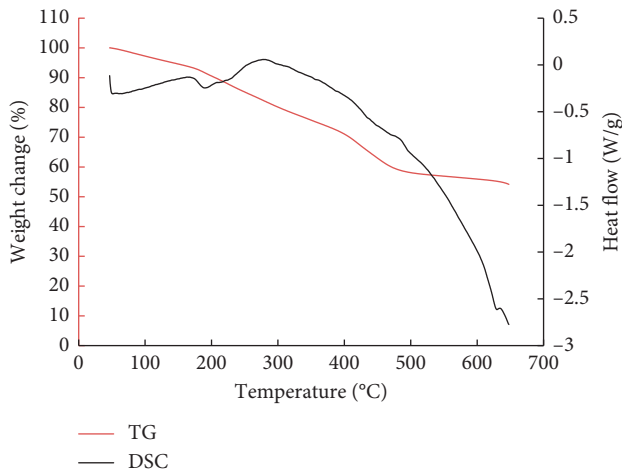


FIGURE 5: TG-DSC measurement of the final product.

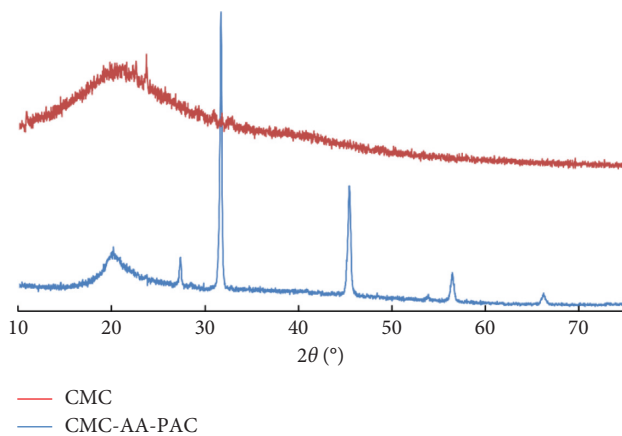


FIGURE 6: X-ray diffraction spectra of products.

indicates that sodium carboxymethyl cellulose has a non-crystal polymerization structure. A further observation of the spectra of the final product reveals that strong diffraction peaks show up near  $32^\circ$ ,  $45^\circ$ , and  $57^\circ$  after a series of reactions, which correspond to the characteristic peaks of NaCl formed by the bonding of chloride ions in poly-aluminum chloride and sodium ions in sodium carboxymethyl cellulose. Compared to the raw material, the final product shows a sharper diffraction peak near  $20^\circ$ , and we obtained the experimental conclusion consistent with 3.2 that the graft copolymerization of CMC, AA, and PAC functional groups occurred. This makes the structure of the resulting product more reinforced, yielding a compact amorphous noncrystal [28].

**3.5. SEM Analysis.** Figure 7 shows the SEM results. An examination of the final product surface in Figures 7(a)–7(c) indicates that, after the cross-linking reaction, the monomers form a tight structure through the impact of the cross-linking agent. Also, there exist many pores on the surface, which (1) greatly increases the contact area with the shotcrete layer, leading to an enhanced adhesive force between the product and the concrete and (2) bolsters the product's

ability to infiltrate into the concrete, i.e., the product can tightly wrap around the concrete and decently cement together the concrete pieces through its occupation of the pore space. Note that the observed rod-shaped and cubic substance on the surface could be the product or what the self-polymerization of monomer generates; besides, the uneven surface of the product gives rise to numerous tiny spaces, which increases the specific surface area, making the adsorption of dust easier [29, 30]; Figure 7(d) shows the cross section of the final product, which indicates that the internal structure of the product is equally compact, and the cross section exhibits a ladder-like structure. This proves that the product has been tightly cemented together before the damage occurs. As such, a strong force is needed to break up the product, and consequently the cross section shows a ladder-like structure.

One can tell from the SEM images that the structure of the final product is relatively compact. After spraying over the roadway, the product can securely wrap around the roadway wall, forming a hardened “shell.” Meanwhile, its large specific surface area allows it to contact more dust, leading to a decent dust-cementing effect.

### 3.6. Reinforcement Experiment Analysis

**3.6.1. Tensile Strength Analysis.** During the experiment, it is found that the amount of the cross-linking agent has a striking impact on the tensile strength of the formed film. Therefore, Figure 8 shows the result derived from tests on measuring the tensile strengths associated with various amounts of the cross-linking agent. The measurement result is roughly consistent with what the plot of film hardness shows. The increase of cross-linking agent amount causes the tensile strength to go up considerably. When the amount of the cross-linking agent reaches an optimal level, it takes 51.2 N of force to break the film. As we further increase the cross-linking agent amount, since most of the coordination reactions have been completed, the surplus cross-linking agent is distributed in the solution as ions. As such, after the desiccation of the solution, the resulting tensile strength trends downward.

The experimental results indicate that the formed film has a decent strength, allowing it to tightly fix the sprayed cement on the roadway. Meanwhile, the product works jointly with anchors to keep the loose rock pieces in place, preventing the sprayed cement from cracking and detaching. This helps maintain the triaxial stress state deep inside the rock formation and enhance the load-bearing capability of the shotcrete layer and the surrounding rock. Also, the deformation and displacement of the roadway surrounding rock due to the internal force is reduced [31].

**3.6.2. Adhesion Analysis.** Figure 9(a) shows the state of the final product after the test. At  $25^\circ\text{C}$ , an NDJ-1 rotary viscometer with #2 rotor is employed to measure the viscosity coefficient of the product, which shows that the viscosity ranges between 60 and 100 mPa·s. One can tell from the

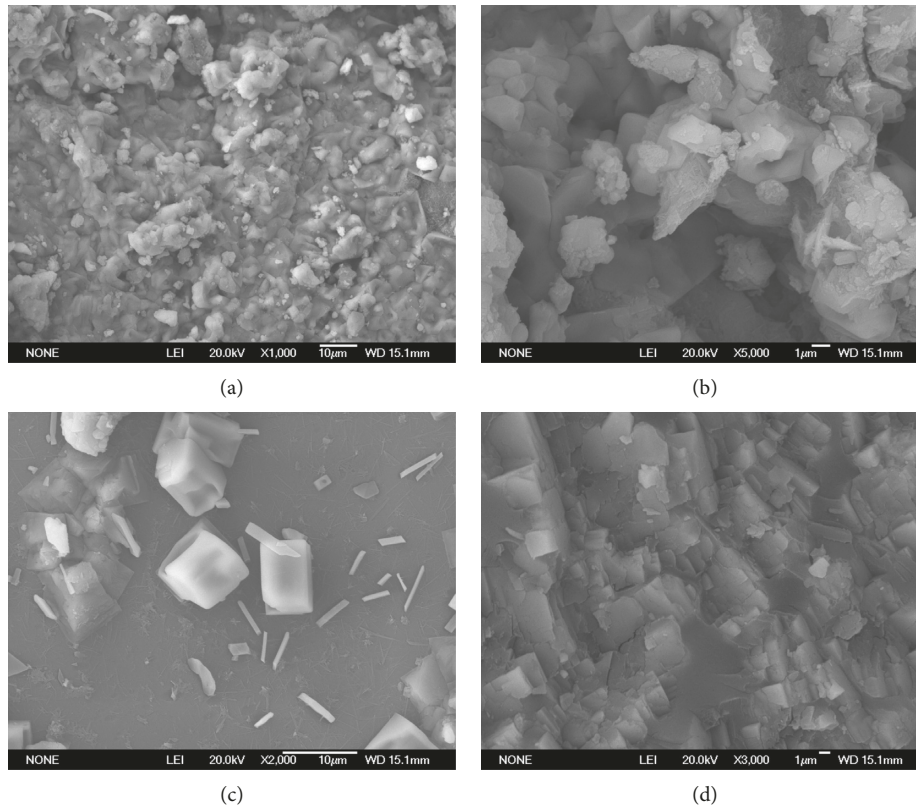


FIGURE 7: SEM images of the final product: (a–c) final product surface; (d) final product cross section.

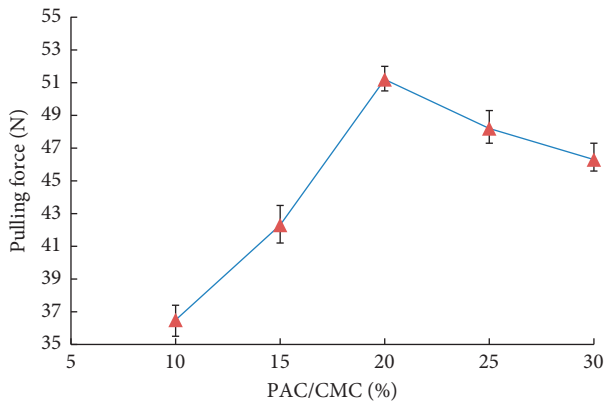


FIGURE 8: Influence factors of tensile strength.

experimental results and the final appearance of the product that the product presents itself as a viscous and light yellowish fluid after the test. This gives the product a strong adhesive force to stick to the roadway [32].

Figure 9(b) uses a tensile testing machine to indicate the force it takes to destroy the cemented structure with various amounts of the product applied. With an increase of the product amount, the force it takes to destroy the cemented structure also increases. As the force peaks, a further increase of the product amount does not cause the force to increase further. This is due to the fact that the bond between the product and the concrete slabs and the intrinsic strength of the product both has peaked.

This test indicates that a strong adhesive force exists between the product and the concrete, which can reach 1.1 MPa. This force includes two parts, i.e., the bond between the product and the concrete shotcrete surface and the cementing effect of the product infiltrating into the cracks of the concrete. This can not only ensure a synchronized displacement under stress but also enhance the cohesion of the joints, leading to a unified load-bearing arch that can basically meet the need of the roadway surrounding rock reinforcement.

*3.6.3. Anticompression and Antibending Experiment Analysis.* Figure 10 is experimental product morphology. An examination of the data collected from the testing machine shows in Table 2 that when the compressive displacement is merely 1.49 mm, a peak compressive force of 602 N is recorded. This indicates that the product's deformation is 1.42 mm while withstanding a stress of 2.64 MPa; during the antibending test, it takes 236 N force to break the product. This illustrates the enhanced load-bearing capability of the roadway and the shotcrete layer under triaxial stress state with the surface treatment of the product. Under the influence of the external force, the original triaxial stress state can be transformed into uniaxial stress state or biaxial stress state, making the load-bearing capability of the surrounding rock and the shotcrete layer reduced. This can cause collapse of the structure and the detachment of the shotcrete layer. The product can infiltrate into the soft and

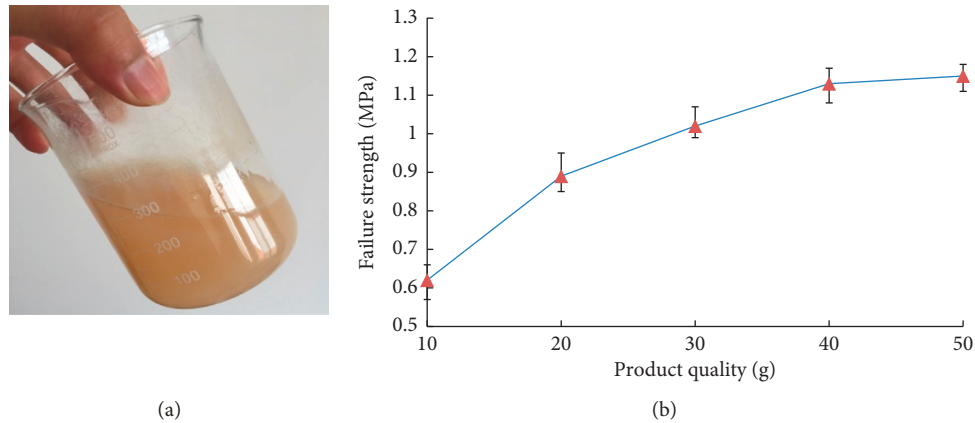


FIGURE 9: Experimental results of adhesion: (a) the state of the final product; (b) effect of product quality on adhesion.



FIGURE 10: Experimental product morphology.

broken joints in the rock and shotcrete layer as well as forming an external layer of high-strength thin film, which can turn the deformation state back into the original triaxial stress state. As such, a reinforcement of the surrounding rock is attained.

### 3.7. Dust-Cementing Test Analysis

**3.7.1. Dust-Cementing Analysis.** Figure 11 is different forms of products. The product surface has many protrusions and cracks, giving the product a strong ability to absorb roadway dust. As shown in Table 3, when 3 grams of coal powder is applied to the product surface, the product can absorb a portion of the dust. As the airflow velocity increases, the adhesion and cementing effect between the coal powder and the product is not enough to withstand the wind, leading to a loss of coal powder. Due to the coarse surface morphology of the product, a large portion of the

coal powder is permanently fixed to the surface of the product; a product subject to 3-day desiccation has more water on the surface compared to a product with 7-day desiccation. The presence of water also helps enhance the dust absorption effect [33].

**3.7.2. CCD Imaging Analysis.** Figure 12 is an industrial camera experimental photo. One can tell from the CCD images that, after a three-day desiccation, the product's surface can retain a large amount of dust. The black sizable chunks of dust indicate the remarkable cementing effect due to the presence of water. At the other places on the surface, the existence of cracks on the surface can also fix certain amount of dust. Due to the humid environment in the underground mine, the application of the product to the roadway yields similar effect with the product subject to 3-day desiccation. Through a statistical calculation,  $1 \text{ m}^2$  of the thin spray material can absorb 50 grams of coal powder, indicating that the absorption effect is fairly satisfactory. This can help reduce the dust entrained in the roadway airflow and improve the working environment.

## 4. Conclusion

The present experiment conducts a suite of molecular modification reactions involving sodium carboxymethyl cellulose, acrylic acid, and polyaluminum chloride so as to produce a high-strength thin spray material suitable for reinforcing the surrounding rock of roadway and cementing dust. The infrared spectroscopy test indicates that the acrylic acid is grafted to the carboxymethyl cellulose, and a coordination chelating reaction occurs between the acrylic acid and the polyaluminum chloride. The thermogravimetric analysis indicates that the product can maintain a decent thermal stability in the subsurface environment; the SEM experiment shows that the product can deliver a strong adhesive force and a compact molecular structure; and through a suite of single-factor experiments, it is determined that the optimal formula is sodium carboxymethyl cellulose: acrylic acid = 5 : 8, initiator: acrylic acid = 2.0%, and cross-linking agent: sodium carboxymethyl cellulose = 1 : 5. The

TABLE 2: Experimental result.

Project	Force value (N)	Peak value (N)	Displacement (mm)	Deformation (mm)	Strength (MPa)
Compress	460.32	901.63	1.49	1.42	2.64
Bend	126.05	235.56	10.16	2.02	0.748

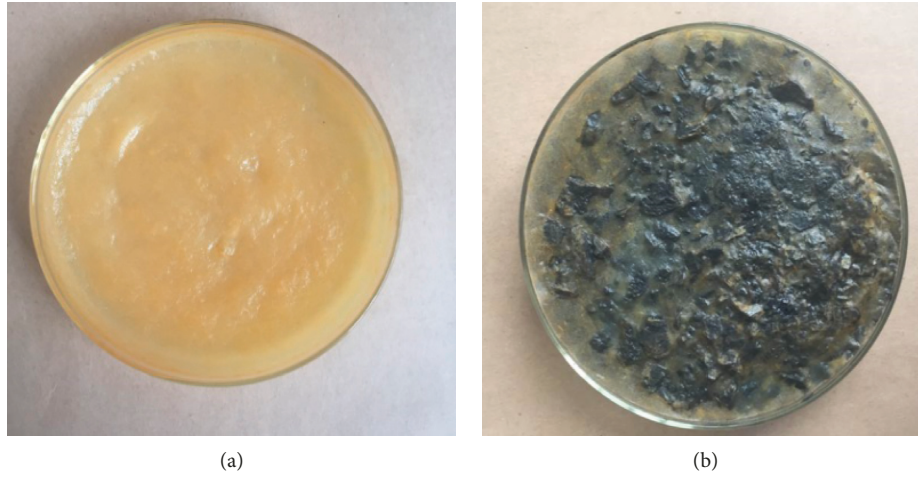


FIGURE 11: Different forms of products: (a) 3 days of drying; (b) 7 days of drying.

TABLE 3: Effect of dust adhesion under different wind speeds.

Wind speed	1 m/s	2 m/s	3 m/s	4 m/s	5 m/s	6 m/s
3 days of drying	2.21 g	1.56 g	1.33 g	1.26 g	1.21 g	1.20 g
Percentage of weight gain	111.05%	107.80%	106.65%	106.30%	106.5%	106.00%
7 days of drying	1.89 g	1.44 g	1.28 g	1.11 g	0.98 g	0.91 g
Percentage of weight gain	109.45%	107.20%	106.40%	105.55%	104.9%	104.55%

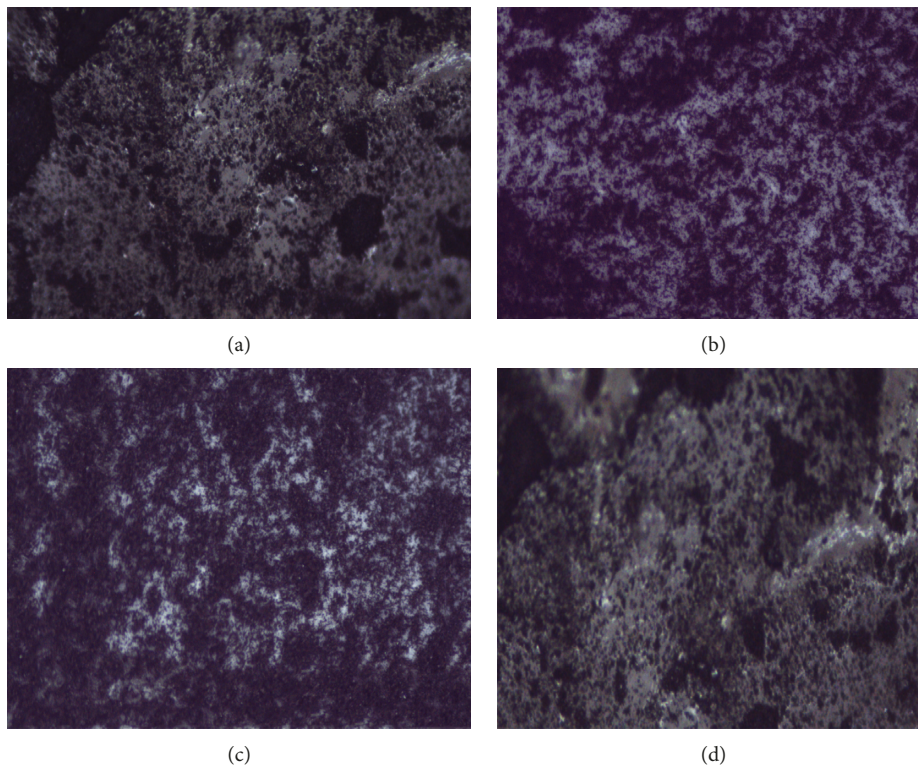


FIGURE 12: Industrial camera experimental photo.

optimal reaction temperature is 50°C. A characterization of the product indicates that the formed film has a high hardness, reaching 96 HA. Also, it can deliver a good antiweathering performance, and a study on the tensile strength and cementing effect of the product indicates that the product can infiltrate into the soft and broken joints in the rock. This leads to a strong mechanical strength and an adjusted stress state in the rock, which reinforces the surrounding rock; an analysis of the product's dust-cementing effect shows that the product has a strong ability to absorb dust, which can help mitigate the issue concerning the excessive airflow-entrained dust in the mine. Also, the developed product has a strong strength and low cost, making it favorable to apply to the field.

### Conflicts of Interest

The authors declare that they have no conflicts of interest.

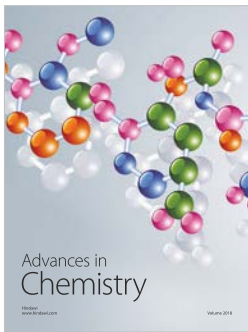
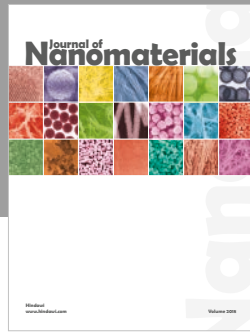
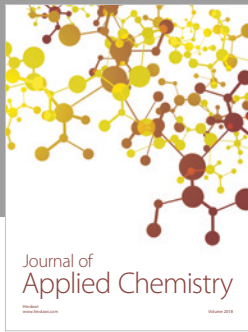
### Acknowledgments

This work was financially supported by the National Key Research and Development Program of China (Grant no. 2017YFC0805202), the National Natural Science Foundation of China (Grant nos. 51774198 and 51474139), the Outstanding Youth Fund Project of Provincial Universities in Shandong Province (Grant no. ZR2017JL026), the Qingdao City Science and Technology Project (Grant no. 16-6-2-52-nsh), the Natural Science Foundation of Shandong Province (Grant no. ZR2016EEM36), and the Qingdao Postdoctoral Applied Research Project (Grant no. 2015194).

### References

- [1] G. Ni, Z. Li, and H. Xie, "The mechanism and relief method of the coal seam water blocking effect (WBE) based on the surfactants," *Powder Technology*, vol. 323, pp. 60–68, 2018.
- [2] T. Sasaoka, T. Karian, A. Hamanaka, H. Shimada, K. Matsui, and M. Ichinose, "Effect of mine water on the stability of underground coal mine roadways," *Geotechnical and Geological Engineering*, vol. 34, no. 2, pp. 671–678, 2016.
- [3] Z.-X. Hu, X.-M. Hu, W.-M. Cheng, Y.-Y. Zhao, and M.-Y. Wu, "Performance optimization of one-component polyurethane healing agent for self-healing concrete," *Construction and Building Materials*, vol. 179, pp. 151–159, 2018.
- [4] Y. Wei, X. Miao, J. Zhang, and S. Zhong, "Mechanical analysis of effective pressure relief protection range of upper protective seam mining," *International Journal of Mining Science and Technology*, vol. 27, no. 3, pp. 537–543, 2017.
- [5] G. Wang, M. Wu, R. Wang, H. Xu, and X. Song, "Height of the mining-induced fractured zone above a coal face," *Engineering Geology*, vol. 216, pp. 140–152, 2017.
- [6] G. H. Ni, K. Dong, S. Li, and Q. Sun, "Gas desorption characteristics effected by the pulsating hydraulic fracturing in coal," *Fuel*, vol. 236, pp. 190–200, 2019.
- [7] G. Zhou, Q. Zhang, R. Bai, T. Fan, and G. Wang, "The diffusion behavior law of respirable dust at fully mechanized caving face in coal mine: CFD numerical simulation and engineering application," *Process Safety and Environmental Protection*, vol. 106, pp. 117–128, 2017.
- [8] W. Y. Guo, Y. L. Tan, F. H. Yu et al., "Mechanical behavior of rock-coal-rock specimens with different coal thicknesses," *Geomechanics and Engineering*, vol. 15, no. 4, pp. 1017–1027, 2018.
- [9] Q. Liu, W. Nie, Y. Hua, H. Peng, and Z. Liu, "The effects of the installation position of a multi-radial swirling air-curtain generator on dust diffusion and pollution rules in a fully-mechanized excavation face: a case study," *Powder Technology*, vol. 329, pp. 371–385, 2018.
- [10] Q. Zhang, G. Zhou, X. Qian, M. Yuan, Y. Sun, and D. Wang, "Diffuse pollution characteristics of respirable dust in fully-mechanized mining face under various velocities based on CFD investigation," *Journal of Cleaner Production*, vol. 184, pp. 239–250, 2018.
- [11] G. H. Ni, H. C. Xie, Z. Li, L. X. Zhuansun, and Y. Y. Niu, "Improving the permeability of coal seam with pulsating hydraulic fracturing technique: a case study in Changping coal mine, China," *Process Safety and Environmental Protection*, vol. 117, pp. 565–572, 2018.
- [12] Z. Li, B. Nocelli, and S. Saydam, "Effect of rock strength and surface roughness on adhesion strength of thin spray-on liners," *International Journal of Rock Mechanics and Mining Sciences*, vol. 91, pp. 195–202, 2017.
- [13] Z. Liu, H. Yang, W. Wang, W. Cheng, and L. Xin, "Experimental study on the pore structure fractals and seepage characteristics of a coal sample around a borehole in coal seam water infusion," *Transport in Porous Media*, vol. 125, no. 2, pp. 289–309, 2018.
- [14] D. P. Mason and T. R. Stacey, "Support to rock excavations provided by sprayed liners," *International Journal of Rock Mechanics and Mining Sciences*, vol. 45, no. 5, pp. 773–788, 2008.
- [15] J. Liu, R. Zhang, D. Song, and Z. Wang, "Experimental investigation on occurrence of gassy coal extrusion in coal mine," *Safety Science*, vol. 113, pp. 362–371, 2019.
- [16] W.-Y. Guo, T.-B. Zhao, Y.-L. Tan, F.-H. Yu, S.-C. Hu, and F.-Q. Yang, "Progressive mitigation method of rock bursts under complicated geological conditions," *International Journal of Rock Mechanics and Mining Sciences*, vol. 96, pp. 11–22, 2017.
- [17] G. Liu, W. Cheng, and L. Chen, "Investigating and optimizing the mix proportion of pumping wet-mix shotcrete with polypropylene fiber," *Construction and Building Materials*, vol. 150, pp. 14–23, 2017.
- [18] L. Chen, P. Li, G. Liu, W. Cheng, and Z. Liu, "Development of cement dust suppression technology during shotcrete in mine of China-A review," *Journal of Loss Prevention in the Process Industries*, vol. 55, pp. 232–242, 2018.
- [19] P. Golshaei, O. Güven, P. Golshaei, and O. Güven, "Chemical modification of PET surface and subsequent graft copolymerization with poly(N-isopropylacrylamide)," *Reactive and Functional Polymers*, vol. 118, pp. 26–34, 2017.
- [20] A. Gosiewska, J. Drelich, J. S. Laskowski, and M. Pawlik, "Mineral matter distribution on coal surface and its effect on coal wettability," *Journal of Colloid and Interface Science*, vol. 247, no. 1, pp. 107–116, 2002.
- [21] T. Fan, G. Zhou, and J. Wang, "Preparation and characterization of a wetting-agglomeration-based hybrid coal dust suppressant," *Process Safety and Environmental Protection*, vol. 113, pp. 282–291, 2018.
- [22] C. Spagnol, F. H. A. Rodrigues, A. G. B. Pereira, A. R. Fajardo, A. F. Rubira, and E. C. Muniz, "Superabsorbent hydrogel composite made of cellulose nanofibrils and chitosan-graft-poly(acrylic acid)," *Carbohydrate Polymers*, vol. 87, no. 3, pp. 2038–2045, 2012.

- [23] H. Ozturk, "Fracture mechanics interpretation of thin spray-on liner adhesion tests," *International Journal of Adhesion and Adhesives*, vol. 34, no. 4, pp. 17–23, 2012.
- [24] P. Mpunzi, R. Masethe, M. Rizwan, and T. R. Stacey, "Enhancement of the tensile strengths of rock and shotcrete by thin spray-on liners," *Tunnelling and Underground Space Technology*, vol. 49, pp. 369–375, 2015.
- [25] D. Guner and H. Ozturk, "Experimental and numerical analysis of the effects of curing time on tensile mechanical properties of thin spray-on liners," *Rock Mechanics and Rock Engineering*, vol. 49, no. 8, pp. 3205–3222, 2016.
- [26] K. Kabiri, H. Omidian, and M. Zohuriaan-Mehr, "Novel approach to highly porous superabsorbent hydrogels: synergistic effect of porogens on porosity and swelling rate," *Polymer International*, vol. 52, no. 7, pp. 1158–1164, 2003.
- [27] M. Modesti, A. Lorenzetti, F. Simioni, and G. Camino, "Expandable graphite as an intumescent flame retardant in polyisocyanurate-polyurethane foams," *Polymer Degradation and Stability*, vol. 77, no. 2, pp. 195–202, 2002.
- [28] W. Cheng, X. Hu, J. Xie, and Y. Zhao, "An intelligent gel designed to control the spontaneous combustion of coal: fire prevention and extinguishing properties," *Fuel*, vol. 210, pp. 826–835, 2017.
- [29] G. Zhou, Y. Ma, T. Fan, and G. Wang, "Preparation and characteristics of a multifunctional dust suppressant with agglomeration and wettability performance used in coal mine," *Chemical Engineering Research and Design*, vol. 132, pp. 729–742, 2018.
- [30] J. Zhang, F. Jiang, J. Yang, W. Bai, and L. Zhang, "Rockburst mechanism in soft coal seam within deep coal mines," *International Journal of Mining Science and Technology*, vol. 27, no. 3, pp. 551–556, 2017.
- [31] H. Yilmaz, "Comparison of tensile-bond strength of thin spray-on liners," *International Journal of Mining, Reclamation and Environment*, vol. 27, no. 1, pp. 56–71, 2012.
- [32] H. Ozturk and D. D. Tannant, "Thin spray-on liner adhesive strength test method and effect of liner thickness on adhesion," *International Journal of Rock Mechanics and Mining Sciences*, vol. 47, no. 5, pp. 808–815, 2010.
- [33] G. Zhou, T. Fan, M. Xu, H. Qiu, J. Wang, and L. Qiu, "The development and characterization of a novel coagulant for dust suppression in open-cast coal mines," *Adsorption Science and Technology*, vol. 36, no. 1-2, pp. 608–624, 2017.



**Hindawi**  
Submit your manuscripts at  
[www.hindawi.com](http://www.hindawi.com)

